PHYSICS OF FLUIDS

https://aip.scitation.org/journal/phf

Accepted August 31st 2022

Electroosmosis Modulated Periodic Membrane Pumping Flow and Particle Motion with Magnetic Field Effects

[1]D. S. Bhandari, [1*]Dharmendra Tripathi and [2]O. Anwar Bég

[1]Department of Mathematics, National Institute of Technology Uttarakhand, Srinagar-246174, India

[2]Professor and Director- Multi-Physical Engineering Sciences Group (MPESG), Dept. Mechanical and Aeronautical Engineering, SEE, Salford University, Manchester, M54WT, UK.

Corresponding author: dtripathi@nituk.ac.in

ABSTRACT

Theoretical studies of micro-electro-mechanical systems (MEMS) provide an important insight into the mechanisms and optimization of such devices for a range of applications including biomedical and chemical engineering. Inspired by emerging applications of microfluidics, unsteady viscous flow in a microchannel with periodic membrane pumping modulated by electro-magnetohydrodynamics, is analysed in a mathematical framework. The membrane kinematics induce the pressure inside the microchannel where electric field enhances the capability of pumping flow rate. This model is formulated based on the Navier–Stokes equations, Poisson equation and the Maxwell electromagnetic equations and further simplified using the lubrication approximations and Debye-Hückel linearization. The transformed dimensionless conservation equations under appropriate boundary conditions are analytically solved and further illustrated the graphical results through MATLAB (2019b) software. From the computational results, it is found that the Hartmann number enhances the fluid pressure uniformly throughout the microchannel, while electric field parameter enforces the direction of pressure-driven flow. Time-averaged flow rate exhibits a linear decay with axial pressure gradient and it is strongly elevated with electric field parameter whereas it is weakly increased with EDL thickness parameter. It is further observed that fluid is driven unidirectionally by the

membrane contractions via a particle tracking simulation method. This study is relevant to provide the parametric estimation in designing the magnetic field-based microfluidics devices for microlevel transport phenomena.

KEYWORDS: *Electroosmotic flow; magnetohydrodynamics; membrane kinematics; particle tracking simulation; streamlines.*

NOMENCLATURE

M	shape of the membrane profile
A	amplitude of membrane contraction
a	half length of the membrane
L	length of the microchannel
λ	width of the microchannel
t	time scale
$\boldsymbol{U_i}$	velocity vector $(u, v, 0\ )$ of the fluid
U_{e0}	reference electroosmotic velocity
Q	volumetric flow rate
$\boldsymbol{F}$	body force
p	pressure of the fluid
J	local ion current density
$\boldsymbol{E}$	applied electrical field
$\boldsymbol{B}$	transverse magnetic field $(0\,, B_0, 0)$
K_B	Boltzmann constant
T_a	averaged temperature of the electrolytic solution
z_i	charge balance
n_0	concentration of ions
e	protonic charge
Greek Symbols	
ε	permittivity of electromagnetic fluid
σ	electrical conductivity
μ	viscosity of the fluid
ρ	density of the fluid
ρ_e	density of charged ions
ψ	stream function
Φ	electric potential
Φ_0	zeta potential
κ	Inverse EDL thickness
Dimensionless parameter	
Re	Reynolds number
δ	amplitude ratio
$\boldsymbol{H_a}$	Hartmann number,
E_T	electric field parameter

l. INTRODUCTION

Micro-electro-mechanical systems (MEMS) are being increasingly deployed in medical and bio-engineering applications due to the excellent integrated functionalities achievable in such systems. A micropump is one of the key features of these systems where electric field can be used to enhance the pumping efficiency. Jeong *et al.* [1] have fabricated a mechanical sensitivity-based peristaltic micropump that achieves a maximum flow rate of about $0.36\mu L/s$. This is particularly relevant to optimizing the transportation of separated cells, moving reagents to the separation/mixing chamber, drug transport, genomic DNA analysis through pneumatic microfluidic pumping [2], and separation techniques in capillary electrophoresis [3]. Based on the characteristics of peristaltic pumping, Forouzandeh *et al.* [4] classified the fluid actuation induced by the peristaltic micropump (PMP). These studies have focused on wave propagation in the flow direction which is referred to as the continuous-scheme PMP [5,6]. Despite their good efficiency, several challenges exist in designing micropumps to deliver consistently high flow rates as well as high-pressure drops.

To induce consistently high flow in microfluidics devices without loss of pressure drop, the deployment of external electric field gradients (electroosmotic flow i. e. EOF) has therefore become increasingly popular in micromechanical systems. Typically, electroosmotic flow [7] involves the generation of an electric double layer (EDL) near the charged surface as a charged solid surface comes into contact with an electrolyte solution. Therefore, when an electric field is imposed, the EDL has induced a bulk fluid flow which is referred to as electroosmotic flow [8]. This non-mechanical mechanism has proven to be the most efficient mechanism for conveying small quantities (micro-volumes) of fluids in microfluidic devices [9]. Most recently, some interesting studies [10-15] on electroosmotic flow (EOF) have been presented in the literature including EOF of viscoelastic fluids with slip-dependent zeta potential [10], evolution from periodic to chaotic AC electroosmotic flows [11], fluid mixing in combined electroosmotic and pressure driven transport [12], EOF of viscoelastic fluids in an isosceles right triangular cross section [13], EOF over high zeta potential modulated surfaces [14] and energy efficiency analysis in oscillatory EOF [15]. These studies have addressed the effects of zeta potential, EDL thickness, fluids properties and geometrical properties in EOF.

Magnetohydrodynamics (MHD) is another key mechanism available for regulating natural transport phenomena and has also been implemented widely in the augmentation of biological

flows [16]. MHD techniques which involve the interaction of an applied magnetic field and electrically conducting fluid media, are also deployed in controlling hemodynamic circulation, biomagnetic tissue thermal therapy, cancer tumour treatment, etc [17-19]. Das et al. [20] developed a novel technique to separate particles-based size in narrow fluidic confinements by studying the combined effects of magnetophoretic and magnetohydrodynamic transport phenomena. According to Chakraborty and Paul [21], a significant increase in volumetric flow rates can be accomplished with a low-magnitude magnetic field. Bhandari *et al.* [22] analysed the hydromagnetic flow induced by the periodic membrane contraction in a two-dimensional finite length channel. In addition, some studies have also focused on the influence of induced magnetic fields in MHD flows [23-25]. These arise when the magnetic Reynolds number is sufficiently high to generate magnetic induction and the flow distorts the magnetic field. With the combination of magnetic and electric fields, electromagnetohydrodynamics (EMHD) has become increasingly popular for more efficiently manipulating fluid flow in micromechanical systems [26-29]. In this regard, a computational fluid dynamics (CFD) simulation of the combined influence of electric and magnetic fields in regulating peristaltic transport of physiological fluids in a microchannel was reported by Ramesh *et al.* [30] in which the effects of Hartmann number and EDL thickness on flow and pumping characteristics were studied. Prakash *et al.* [31] have considered the dual effects of the external electric and magnetic fields in regulating non-Newtonian fluids flow through peristaltic pumping and discussed the flow analysis under the effects non-Newtonian parameters. The use of electromagnetohydrodynamic (EMHD) in precisely controlling peristaltic microflows has been demonstrated in these studies with the applications including limited dilution of samples, improved processing capabilities for separation purposes, etc. Most of the above literature is based on the continuous-scheme PMP.

However, the discrete-scheme PMP can achieve greater reliability via microscale fabrication processes. In response to this essential mechanism, Aboelkassem and Staple [32] have proposed a bioinspired membrane pumping mechanism ("non-propagative" where at least two membranes that operate with time-lag) based on insect respiratory phenomena at the microscale. This bio-inspired mechanism has the potential for pumping the fluid more efficiently with high pressure generated via the periodic membrane motion. In another membrane model, Yasser [33] proposed a single membrane contraction that operates in a "propagative" mode. Furthermore, Bhandari *et al.* [34] extended the Yasser's [33] model to consider couple stress fluids flow under active membrane propulsion. When working fluids are

electro-conductive, the characteristics of membrane pumping may further be enhanced via external electric. Tripathi et al. [35] applied electroosmosis in membrane-based pumping model, and analysed the effects of zeta potential and EDL thickness. Heat transfer analysis with pressure and buoyancy forces for the membrane-based pumping flow model was investigated by Bhandari et al. [36]. Thus far the combined influence of electroosmotic and magnetohydrodynamics in electroconductive membrane pumping has not been examined.

In the present article, a novel mathematical model is developed to examine the unsteady flow of electroconductive fluids in a microchannel with periodic membrane pumping under the effects of magnetic and electric forces. Although some previous studies have considered the fluids flow in microchannel under the combined effects of transverse magnetic field and axial electrical field [26, 27] but they have not addressed the discrete scheme PMP i.e. periodic membrane pumping mechanism. *This is the main objective and novelty of the present investigation.* The influences of key control parameters i.e., Hartmann number, EDL thickness, electric field parameter, etc. are presented graphically. Additionally, fluid particle trajectories inside the microchannel through the periodic membrane contractions is also computed via a particle tracking simulation method. The study finds applications in hybrid lab-on-chip for electro-magnetic microscale pumping process in biomedical sciences and health care.

ll. PROBLEM FORMULATION

A. Geometric model of membrane pumping

The membrane pumping based flow regime is illustrated in **Fig. 1** where the transverse magnetic field and applied electrical field are also applied to regulate the transient viscous flow in microchannel. Membrane pumping is generated on the upper and lower walls of the microchannel. The membrane is periodically propagating over a complete contraction (compression and expansion phases) cycle. The membrane resumes the initial position after completing the contraction cycle and repeats the process without any external force. The mechanism of periodic membrane pumping is mathematically expressed in a cartesian coordinate system as (see Ref. [33]):

$$h^*(x^*,\mathrm{t}^*) = \begin{cases} \frac{\lambda}{2}; & if x^* \in [-\frac{L}{2}, -a^*) \cup (a^*, \frac{L}{2}], \\ \frac{\lambda}{2} + A((\frac{x^*}{a^*})^{2M} - 1)^3 (1 - k_o^* x^* cos(\pi U_{e0}\mathrm{t}^*)) sin^2(\pi U_{e0}\mathrm{t}^*); & if x^* \in [-a^*, a^*], \end{cases} \tag{1}$$

$h^*(x^*, t^*)$ represents the walls of the microchannel with amplitude of membrane contraction (A), k_o^* is optimized for the membrane profile, M is the shape of the membrane profile, length of the micro-channel ranges in $a^* \in \left[-\frac{L}{2}, \frac{L}{2}\right]$, based on the model of Aboelkassem [33].

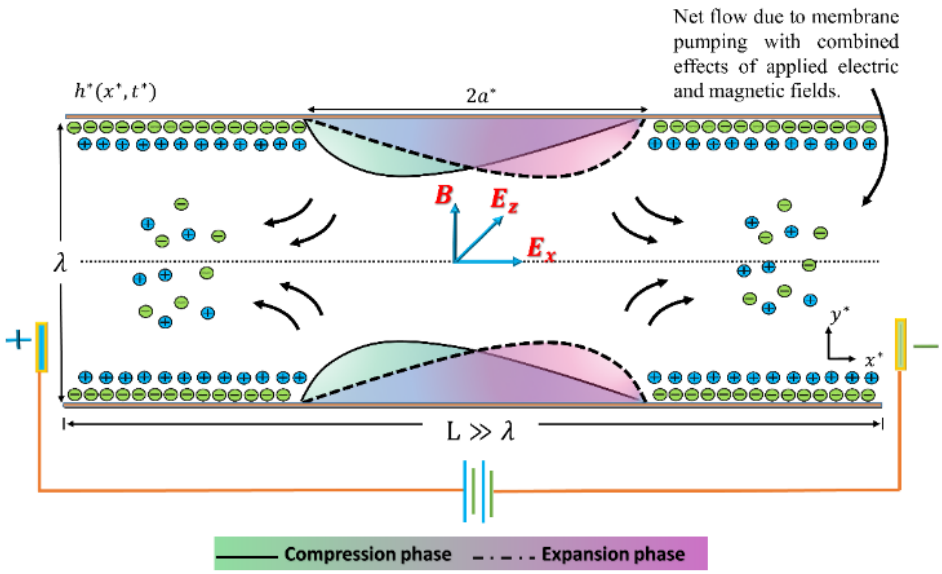

FIG. 1. Schematic diagram of the membrane-based pumping flow model modulated by electroosmosis and magnetohydrodynamics.

B. Theory of electromagnetic field

The Maxwell equation (2) which is composed of the electrical and magnetic effects is used to derive the Lorentz force charge per unit volume that acts on the fluid and is given as:

$$J = \sigma(\boldsymbol{E} + (\boldsymbol{U}_i^* \times \boldsymbol{B})) \qquad \text{(Local ion current density)} \qquad (2)$$

where σ is the electrical conductivity of the channel that quantifies the magnitude of the electrical field $\boldsymbol{E}$ flow through and proportional to the flow velocity $\boldsymbol{U}_i^*$ due to the transverse magnetic field $\boldsymbol{B} = (0, B_0, 0)$. The flow is simultaneously acted upon by a transverse magnetic field and an applied lateral electric field (out of the channel of flow) of strength E_Z, respectively. The $J \times \boldsymbol{B}$ is the electro magneto hydrodynamics and with the help of Ohm's Law it can be calculated as:

$$J \times \boldsymbol{B} = \sigma(\boldsymbol{E} + \boldsymbol{U}_i^* \times \boldsymbol{B}) \times \boldsymbol{B} = \sigma(\boldsymbol{E} + (\boldsymbol{u}^*\boldsymbol{i} + \boldsymbol{v}^*\boldsymbol{j} + \boldsymbol{0k}) \times \boldsymbol{B}) \times \boldsymbol{B} \qquad (3)$$

$$J \times \boldsymbol{B} = \sigma B_0 E_z - \sigma B_0^2 \boldsymbol{u}^*$$

As a result, additional forces are exerted along with the driving axial pressure gradient as a result of the electromagnetic volumetric force $\sigma B_0 E_z$ and a retarding magnetohydrodynamic volumetric force $\sigma B_0^2 \boldsymbol{u}^*$. It is important to note that despite there being no electric field

applied along the axis of the channel, an electric field, specifically the streaming/electric potential field $E_x = \nabla\Phi^*$ is inherently induced by the advection of ionic species with the flow in the microchannel using the electrokinetic phenomenon [21].

C. Electroosmosis

In order to assess the electrokinetic phenomena in the microfluidic system, the attribute of the induced electric field is taken in terms of the EDL potential distribution (Φ^*). The advection of counter-ionic concentration with the flow due to the influence of an EDL that forms near the liquid–wall interface, an electric charge is deposited in the vicinity of the microchannel wall to enhance the potential at the walls. The charge number density is measured by how much electric charge is accumulated in relation to the electric potential via the *Poisson equation as*:

$$\nabla^2\Phi^* = -\frac{\rho_e}{\varepsilon}. \tag{4}$$

Here Φ^* is electric potential, ε is the permittivity of electromagnetic fluid, and $\rho_e = e\bar{z}(n^+ - n^-)$ is the density of charged ions. z is the valence of the ions and $n^{\pm}$ are the number of cations and anions respectively, can be quantified by the Boltzmann distribution as $n_{\pm} = \mathrm{n}_0\exp(\mp\bar{z}e\Phi^*/\mathrm{k}_\mathrm{B}T_a)$ which is valid when the flow of the Peclet number is sufficiently small [26]. In such a case, the net charge density in a unit volume of the fluid is expressed as

$$\rho_e = 2n_0 e\bar{z}\, sinh\left(\frac{ez\Phi^*}{K_B T_a}\right), \tag{5}$$

$e, \bar{z},\ n_0$ denote respectively, the protonic charge, charge balance, and the concentration of ions in the bulk flow. K_B is the Boltzmann constant, and T_a is the average temperature of the electrolytic solution.

The parallel walls are assumed to be charged and bear a uniform zeta potential of Φ_0 at the wall, which is smaller than thermal potential i.e., $|\bar{z}e\Phi^*| < |k_B T_a| \rightarrow \Phi^* \ll 1$. Using the linear Debye-Huckel approximation, viz, $sinh\left(\frac{e\bar{z}\Phi^*}{K_B T_a}\right) \approx \frac{e\bar{z}\Phi^*}{K_B T_a}$, the electric potential distribution due to the presence of the EDL is described by the Poisson-Boltzmann equation that can be expressed as:

$$\frac{\partial^2\Phi^*}{\partial x^{*2}} + \frac{\partial^2\Phi^*}{\partial y^{*2}} = -2n_0 e z_i\left(\frac{e z_i\Phi^*}{\varepsilon K_B T_a}\right), \tag{6}$$

subjected to the following boundary conditions:

$$\Phi^*|_{y^*=h^*} = \Phi_0, \qquad \left.\frac{\partial\Phi^*}{\partial y^*}\right|_{y^*=0} = 0, \tag{7}$$

D. Governing equations of the problem

The basic equations governed the electro-magneto-hydrodynamic (EMHD) flow driven by membrane-based pumping are expressed:

$$\nabla . \boldsymbol{U_i^*} = 0, \tag{8}$$

$$\rho \left(\frac{\partial}{\partial t} + \boldsymbol{U_i^*} . \nabla \right) \boldsymbol{U_i^*} = -\nabla p + \mu \nabla^2 \boldsymbol{U_i^*} + \boldsymbol{F}, \tag{9}$$

where $\boldsymbol{F} = \rho_e E_x + J \times \boldsymbol{B}$ is the body force (combined effects of electric and magnetic cross fields acting on the fluids), and p is the fluid pressure. ρ and μ represent the density and kinematic viscosity of the fluid, respectively. The continuity, axial and transverse momentum equations are expressed in the Cartesian coordinate system as:

$$\frac{\partial u^*}{\partial x^*} + \frac{\partial v^*}{\partial y^*} = 0, \tag{10}$$

$$\rho \left(\frac{\partial u^*}{\partial t^*} + u^* \frac{\partial u^*}{\partial x^*} + v^* \frac{\partial u^*}{\partial y^*} \right) = -\frac{\partial p^*}{\partial x^*} + \mu \left(\frac{\partial^2 u^*}{\partial x^{*2}} + \frac{\partial^2 u^*}{\partial y^{*2}} \right) + \rho_e E_x + \sigma B_0 E_z - \sigma B_0^2 u, \tag{11}$$

$$\rho \left(\frac{\partial v^*}{\partial t^*} + u^* \frac{\partial v^*}{\partial x^*} + v^* \frac{\partial v^*}{\partial y^*} \right) = -\frac{\partial p^*}{\partial y^*} + \mu \left(\frac{\partial^2 v^*}{\partial x^{*2}} + \frac{\partial^2 v^*}{\partial y^{*2}} \right), \tag{12}$$

subjected to the following boundary conditions:

$$u^*|_{y^*=h^*} = 0, \qquad v^*|_{y^*=h^*} = \frac{\partial h^*}{\partial t^*}, \qquad p^*|_{x^*=L} = p_L$$
$$\left. \frac{\partial u^*}{\partial y^*} \right|_{y^*=0} = 0, \qquad v^*|_{y^*=0} = 0, \qquad p^*|_{x^*=0} = P_0. \tag{13}$$

E. The non-dimensional variables

Reynolds number is the ratio of the inertia force to the viscous force, and it can be defined as: $Re = U_{e0} \rho \lambda / \mu$, where $U_{e0} = -\frac{\varepsilon \Phi_0 E_x}{\mu}$ is the reference electroosmotic velocity. Introducing the following non-dimensional variables: $x = \frac{x^*}{L}, y = \frac{y^*}{\lambda}, t = \frac{t^* U_{e0}}{L}, h = \frac{h^*}{\lambda}, u = \frac{u^*}{U_{e0}}, v = \frac{v^*}{\delta U_{e0}}, p = \frac{p^* \lambda^2}{\mu U_{e0} L}, \Phi = \frac{ze\Phi^*}{k_B T}, \delta = \frac{\lambda}{L}$, the *Poisson-Boltzmann equation* (6) can be written as:

$$\frac{\partial^2 \Phi}{\partial y^2} = \kappa^2 \Phi(y), \qquad \kappa = \lambda \sqrt{\frac{2 n_0 e^2 z_i^2}{K_B T_a \varepsilon}}, \tag{14}$$

where $1/\kappa$ represents the EDL thickness where κ is the ratio of the characteristic transverse length to the Debye length. Equation (14) can be solved using associative electric potential boundary condition given as:

$$\Phi|_{y=h} = \Phi_0, \qquad \left.\frac{\partial \Phi}{\partial y}\right|_{y=0} = 0. \tag{15}$$

The volumetric net charge density ρ_e is derived as:

$$\rho_e = -\varepsilon\kappa^2\Phi_0 \frac{cosh(\kappa y)}{cosh(\kappa h)}. \tag{16}$$

Introducing the non-dimensional variables in Eqs.(10-12) and employing the lubrication approximation, i.e., low Reynolds number ($Re \ll 1$) and width of the microchannel is much lesser than characteristic length ($\lambda \ll L$), neglecting the nonlinear terms in the limits $\delta \ll 1$, and further substituting the expression for volumetric net charge density from Eq.(16), the reduced continuity and momentum equations are rewritten as:

$$\frac{\partial u}{\partial x} + \frac{\partial v}{\partial y} = 0, \tag{17}$$

$$\frac{\partial p}{\partial x} = \frac{\partial^2 u}{\partial y^2} + \kappa^2 \frac{cosh(\kappa y)}{cosh(\kappa h)} + \boldsymbol{H_a^2} E_T - \boldsymbol{H_a^2} u, \quad \frac{\partial p}{\partial y} = 0. \tag{18}$$

The electromagnetic parameters arising in Eqns. (17) - (18) are as follows: $\boldsymbol{H_a} = B_0\, \lambda \sqrt{\frac{\sigma}{\mu}}$ is the Hartmann number, $E_T = -\frac{E_z}{U_{e0} B_0}$ is the electric field parameter. In the axial momentum Eqn. (18), the second term on the right-hand side represents the *volumetric momentum generation caused by the electric potential*, which is induced by electroosmotic flow. The third term represents the *combined effect of the electrical and magnetic body forces*, and the last term is the *Lorentzian magnetic drag generated by the transverse magnetic field*. From Eqn. (18), it is inferred that the pressure is an independent function of y (i.e., $\partial p/\partial y = 0$) since terms of $O(Re\delta)$ and higher-order are neglected. The associated boundary conditions are reduced in the following forms:

$$\begin{aligned} &u|_{y=h} = 0, \qquad v|_{y=h} = \frac{\partial h}{\partial t}, \qquad p|_{x=L} = p_L \\ &\left.\frac{\partial u}{\partial y}\right|_{y=0} = 0, \qquad v|_{y=0} = 0, \qquad p|_{x=0} = p_0 \end{aligned} \tag{19}$$

Equation (1) demonstrates the mechanism of periodically membrane propagation i.e. compression and expansion phases of the membrane with spatial and temporal respectively, are further represented in non-dimensional form as:

$$h(x,t)=\begin{cases}\frac{1}{2}\,; & if\ x\in\left[-\frac{1}{2},-a\right)\bigcup\left(a,\frac{1}{2}\right]\\ \frac{1}{2}+2\alpha_0((\frac{x}{a})^{2M}-1)^3(1-k_0x\cos(\pi t))\sin^2(\pi t); & if\ x\in[-a,a]\end{cases}, \quad (20)$$

F. Analytical Solutions

Solving the boundary value problem defined by Eqs. (17) & (18), the solution for *the axial velocity* is obtained as:

$$u=\frac{1}{\boldsymbol{H_a^2}}\left(\boldsymbol{H_a^2}E_T-\frac{\partial p}{\partial x}\right)\left(1-\frac{\cosh[\boldsymbol{H_a}y]}{\cosh[\boldsymbol{H_a}h]}\right)+\frac{\kappa^2}{\boldsymbol{H_a^2}-\kappa^2}\left(\frac{\cosh[\kappa y]}{\cosh[\kappa h]}-\frac{\cosh[\boldsymbol{H_a}y]}{\cosh[\boldsymbol{H_a}h]}\right). \quad (21)$$

By considering the continuity equation (17) and the axial velocity (21), the transverse velocity is derived as:

$$v=\frac{1}{\boldsymbol{H_a^2}}\frac{\partial^2 p}{\partial x^2}\left(y-\frac{\sinh[\boldsymbol{H_a}y]}{\boldsymbol{H_a}\cosh[\boldsymbol{H_a}h]}\right)-\left(E_T-\frac{1}{\boldsymbol{H_a^2}}\frac{\partial p}{\partial x}\right)\left(\frac{\sinh[H_a y]\tanh[\boldsymbol{H_a}h]}{\cosh[\boldsymbol{H_a}h]}\right)\frac{\partial h}{\partial x} \quad (22)$$
$$+\frac{\kappa^2}{\boldsymbol{H_a^2}-\kappa^2}\left(\frac{\sinh[\kappa y]\tanh[\kappa y]}{\cosh[\kappa h]}-\frac{\sinh[\boldsymbol{H_a}y]\tanh[\boldsymbol{H_a}y]}{\cosh[\boldsymbol{H_a}h]}\right)\frac{\partial h}{\partial x}.$$

Considering the transverse velocity subjected to the boundary condition (i.e., $v|_{y=h}=\frac{\partial h}{\partial t}$), a correlation between the membrane motion and the axial pressure gradient can also be obtained as follows:

$$\frac{\partial h}{\partial t}=\frac{1}{\boldsymbol{H_a^2}}\frac{\partial^2 p}{\partial x^2}\left(\frac{\boldsymbol{H_a}h-\tanh[\boldsymbol{H_a}h]}{\boldsymbol{H_a}}\right)-\frac{\partial h}{\partial x}\left(E_T-\frac{1}{\boldsymbol{H_a^2}}\frac{\partial p}{\partial x}\right)\tanh^2[\boldsymbol{H_a}h] \quad (23)$$
$$-\frac{\kappa^2}{\boldsymbol{H_a^2}-\kappa^2}(\tanh^2[\boldsymbol{H_a}h]-\tanh^2[\kappa h])\frac{\partial h}{\partial x}.$$

Integration of Eqn. (23) with respect to *x*, the *pressure gradient* is derived as:

$$\frac{\partial p}{\partial x}=\left\{G_0(t)+\int_0^x\frac{\partial h(s,t)}{\partial t}ds-\frac{\kappa^2}{\boldsymbol{H_a^2}-\kappa^2}\left(\frac{\tanh[\boldsymbol{H_a}h]}{\boldsymbol{H_a}}-\frac{\tanh[\kappa h]}{\kappa}\right)\right. \quad (24)$$
$$\left.+E_T\left(\frac{\boldsymbol{H_a}h-\tanh[\boldsymbol{H_a}h]}{\boldsymbol{H_a}}\right)\right\}\left(\frac{\boldsymbol{H_a^3}}{\boldsymbol{H_a}h-\tanh[\boldsymbol{H_a}h]}\right).$$

The pressure gradient is a function of both temporal coordinate (*t*) and axial coordinate (*x*), and $G_0(t)$ is calculated over the finite length of the microchannel as:

$$G_0(t) = \int_0^1 \frac{\boldsymbol{H_a}h - \tanh[\boldsymbol{H_a}h]}{\boldsymbol{H_a^3}} dx \Bigg((p_L - p_0) - \int_0^1 \frac{\boldsymbol{H_a^3}}{\boldsymbol{H_a}h - \tanh[\boldsymbol{H_a}h]} \Bigg(\int_0^x \frac{\partial h(s,t)}{\partial t} ds - \frac{\kappa^2}{\boldsymbol{H_a^2} - \kappa^2} \left(\frac{\tanh[\boldsymbol{H_a}h]}{\boldsymbol{H_a}} - \frac{\tanh[\kappa h]}{\kappa} \right) + E_T \left(\frac{\boldsymbol{H_a}h - \tanh[\boldsymbol{H_a}h]}{\boldsymbol{H_a}} \right) \Bigg) dx \Bigg). \tag{25}$$

The *pressure distribution* is evaluated as:

$$p = p_0 + \int_0^x \frac{\partial p(s,t)}{\partial x} ds. \tag{26}$$

The dimensionless stream function ($\psi = \int u dy - \int v dx$) is computed as:

$$\psi = \left(\boldsymbol{H_a^2} E_T - \frac{\partial p}{\partial x} \right) \frac{1}{\boldsymbol{H_a^2}} \left(y - \frac{\sinh[\boldsymbol{H_a}y]}{\boldsymbol{H_a}\cosh[\boldsymbol{H_a}h]} \right) + \frac{\kappa^2}{\boldsymbol{H_a^2} - \kappa^2} \left(\frac{\sinh[\kappa y]}{\kappa \cosh[\kappa h]} - \frac{\sinh[\boldsymbol{H_a}y]}{\boldsymbol{H_a}\cosh[\boldsymbol{H_a}h]} \right). \tag{27}$$

The pumping flow is characterized by a volumetric flow rate $Q(x,t)$ which is a function of the pressure gradient. $Q(x,t)$ is calculated by integrating the *axial velocity* over the width of the microchannel ($y = 0$ to $y = h$) which yields as:

$$Q = \left(\boldsymbol{H_a^2} E_T - \frac{\partial p}{\partial x} \right) \frac{1}{\boldsymbol{H_a^2}} \left(h - \frac{\tanh[\boldsymbol{H_a}h]}{\boldsymbol{H_a}} \right) + \frac{\kappa^2}{\boldsymbol{H_a^2} - \kappa^2} \left(\frac{\tanh[\kappa h]}{\kappa} - \frac{\tanh[\boldsymbol{H_a}h]}{\boldsymbol{H_a}} \right). \tag{28}$$

lll. RESULTS AND DISCUSSIONS

A. Parameter selection

The expressions derived for the flow characteristics in section 2 are used to compute axial velocity profile, pressure distribution, volumetric flow rate, and pumping characteristics at a fixed value of $M = 2, a = 0.2, \alpha_0 = 0.2$, and $k_0 = 1.95$, and $t = T/4 \; and \; 3T/4$. The influence of various parameters such as the Hartmann number ($\boldsymbol{H_a}$), electrical field parameter (E_T), inverse EDL thickness (κ), and membrane shape parameter (M) on the above physical quantities are visualized graphically by using MATLAB software. Firstly, the permissible ranges of relevant physical parameters are defined. Here, the typical values of the sundry parameters for the microscale fluid flow with dynamic viscosity $\mu \sim 10^{-3}\, Pa.s$, electric

conductivity $\sigma \sim 2.2 \times 10^{-4}\ S.m^{-1}$, applied magnetic field $B \sim 0.018 - 0.44T$ [37], range of Hartmann numbers i.e. $\boldsymbol{H_a} \sim 0 - 8$ are considered [38]. The potential of the applied electric field ranges as $E \sim 0 - 20\ V/m$ and the electroosmotic velocity is taken as $U_{eo} \sim 100\ \mu m/s$. For the length $\lambda \sim 300 \mu m$ and width $a \sim 100 \mu m$, the value of the inverse EDL thickness is considered as $\kappa \sim 1{,}5\ 10$, and ∞ [27]. An important limitation for microchannel flow is that the magnitude of the lateral electric field should not be too large, otherwise the induced transverse flow will not be neglected, which will contradict the assumption of unidirectional flow [35]. Therefore, the maximum magnitude of the electric field is taken up to 2.

B. Electric potential

The electric potential is crucial in diverse fields including MEMS and technological processes at the micro scale. The electric double layer (EDL) thickness is one of the most important characteristics of electroosmotic flow which affects the electric potential, physicochemical properties of electrolyte solutions, the extent of stability of colloidal systems, etc. Poisson–Boltzmann theory helps to understand the significance of the colloidal dispersions (i.e., zeta potential) and EDL thickness for the dispersion of the electric field. **Fig. 2a** represents the influence of inverse EDL thickness (κ) on the electric potential. The electric potential (Φ) is slightly ascent with the order of κ i.e. surface potential which may cause either a decrease or an increase of the effective EDL thickness. However, $\kappa = \lambda \left(\frac{2n_0 e^2 z_i^2}{K_B T_a \varepsilon}\right)^{1/2}$ increases the physical properties of the particle in the interfacial layer, lead to the enhancement in the electric potential is shown in **Fig. 2a**. Further, the distribution of the electric potential across the microchannel for different values of zeta potential is sketched in **Fig. 2b**. The uniform electric field is regulated in the microchannel except in the membrane region. This means that the electric potential increases as the wall surface interact with the charged particles due to the membrane compression. Another hand, zeta potential provides excess charge due to the colloidal dispersion at the wall surface.

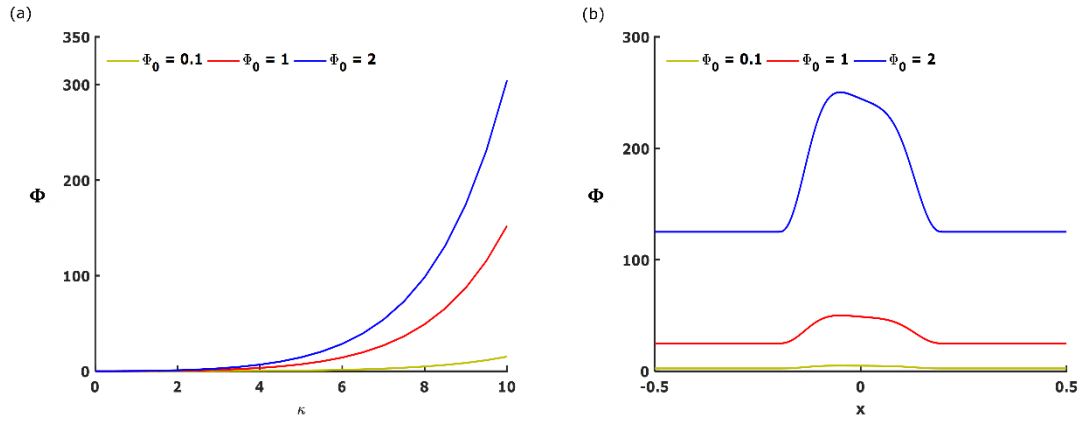

FIG. 2. The variation in the electric potential for different values of wall zeta potential with (a) the inverse EDL thickness and (b) the microchannel length.

C. Fluid pressure and velocity

The contraction of the membrane in the upper half microchannel at fixed times $t = T/4$ is presented in **Fig. 3**. This membrane contraction profile generates the pressure (p) inside the microchannel in the range of $x \in [-0.2, 0.2]$ which can effectively propagate fluids in microchannel. Corresponding to the membrane motion, the spatial variation in the fluid pressure (p) during the contraction phase ($t = T/4$) for different values of the sundry parameters is discussed through contour plots in **Figs. 3 and 4**. Moreover, the corresponding flow field of the velocity vector throughout the microchannel represents the direction of the flow. Here, it is observed that the fluid pressure is constant at each cross-section region within the microchannel. However, the kinematics of the periodic membrane generates uniform pressure distribution on both sides of the contraction region as shown in **Fig. 3a**. The flow field of the velocity vector is stagnated at the centre which bifurcates the fluid in both directions [34]. In addition to the magnetic force, there is an opposing volumetric force of magnitude $\sigma B_0^2 \boldsymbol{u}^*$ which acts to retard axial pressure gradient. In **Fig. 3a**, the Hartmann number ($\boldsymbol{H_a} = 5$) creates a strong Lorentzian force that controls the direction of the fluid velocity. Although, the magnitude of the fluid pressure remains the same for the $\kappa = 3$ as presented in **Fig. 3b**. However, the distribution of the fluid pressure is affected by the EDL thickness i.e. the axial pressure gradient is decreasing with the increment of the κ (i.e. reduction in EDL thickness). The electrical field parameter ($E_T = 2$) enhances the velocity of the fluid, resulting in the decrement of the pressure after the mid-region. Physically, the influence of the magnetic force modifies the strength of the flow, while the electric field enforces the direction of the flow field as shown in **Fig. 4a**. It is

observed the effect of the electric-magnetic fields in the thinner electric double layer, mobilizing greater ionic diffusion and accelerating the pressure, and reducing the flow field as shown in **Fig. 4b**. From this result, it is noted here that the membrane kinematics generates pressure inside the microchannel, while the Hartmann number controls the velocity of the fluid uniformly and the electric field enforces the direction of the flow while EDL improves the pressure-driven flow.

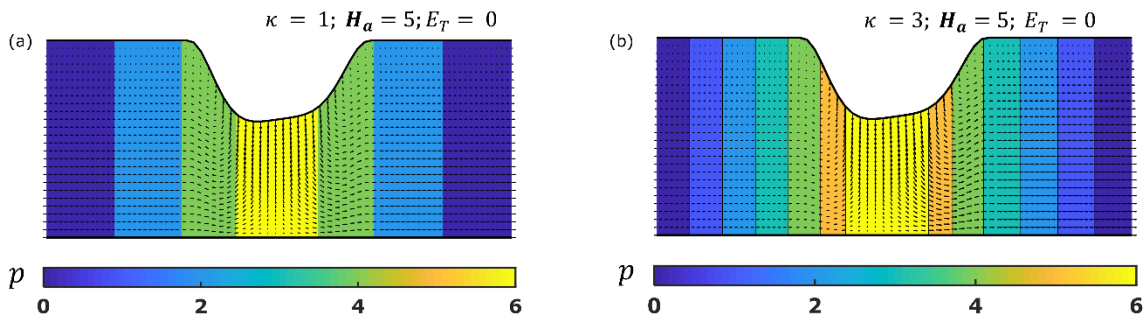

FIG. 3. The contour plot for distribution of pressure through the microchannel with velocity vector flow field without the electric field (a) $k = 1$ & (b) $k = 3$ at fixed values of $\boldsymbol{H_a} = 5$, and $M = 2$.

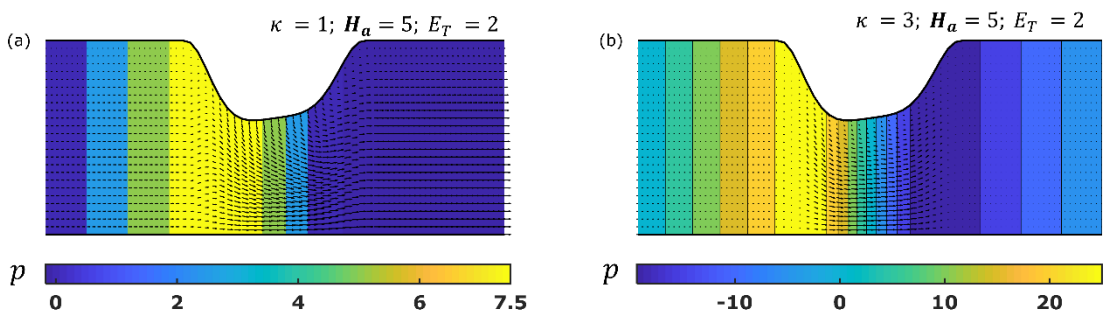

FIG. 4. The contour plot for distribution of pressure through the microchannel with velocity vector flow field with the electric field (a) $k = 1$ & (b) $k = 3$ at fixed values of $\boldsymbol{H_a} = 5$, and $M = 2$.

Figs. 5(a & b) visualize the pressure distributions along the microchannel with different Hartmann numbers ($\boldsymbol{H_a}$) and electric field parameter (E_T) at time $t = T/4$. The pressure at the inlet and outlet of the microchannel is zero, and maximum in the contraction region i.e. $x \in [-0.2, 0.2]$ due to the membrane compression. In **Fig. 5a**, the large value of the Hartmann number is raised the fluid pressure, particularly in the contraction domain as the magnetic force is maximum in this region. For the electric field ($E_T = 2$), the static pressure distribution is

accumulated within the half region (i.e. $x \in [-0.5,0]$). It suddenly decreases and attains the lowest value in the region $x \in [0, 0.5]$ as shown in **Fig. 5b**. In addition, the Hartmann number increases the fluid pressure i.e. stronger magnetic field produces an accentuation in magnetic pressure and distributes the uniform pressure throughout the microchannel. Another hand, the transverse magnetic field regulates the pressure-driven flow and improves the efficiency of the mechanical system**.**

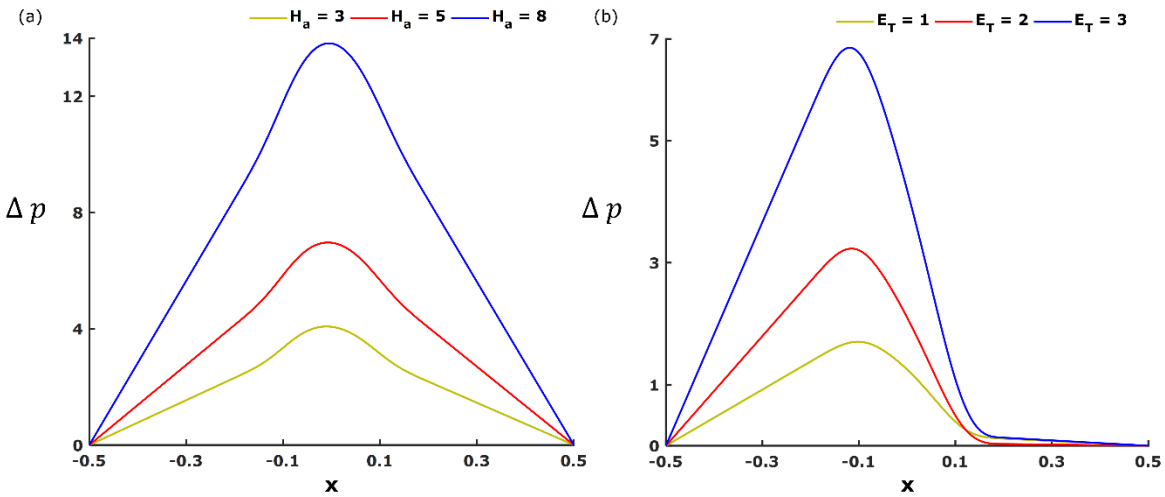

FIG. 5. The pressure distribution along the microchannel for different values of (a) Hartmann number (b) electric field parameter at fixed values of $t = T/4,\ \kappa = 1\ and\ M = 2$.

Figs. 6(a & **b)** represent the impact of the electric field parameter and inverse EDL thickness on the axial velocity profiles during the compression phase ($t = 3T/4$) at position $x = -0.1$. At the walls, the axial velocity is zero due to the no-slip boundary condition, and the maximum axial velocity of the fluid is achieved at the center of the microchannel. In addition, the electric field parameter enhances the movement of the fluid so that the axial velocity profile is increasing with the E_T as presented in **Fig. 6a**. Here, the positive value of the axial velocity component indicates that the fluid is propelled in the forward direction. The κ changes the shape of the axial velocity component inside the microchannel (i.e., the aqueous fluid is inversely affected by the surface charge density of the EDL) as presented in **Fig. 6b**. The high EDL thickness ($\kappa = 2$) ensures negligible electro-viscous effects which lead to axial velocity profile to remain parabolic. As reducing the EDL thickness, the shape of velocity profile is shifting from parabolic to trapezoidal, and further the magnitude of velocity is closer to the walls of the microchannel which is distributed more uniform throughout the channel to maintain the controlled movement. When EDL thickness is minimum ($\kappa \rightarrow \infty$), the trend of

velocity profile is further shifting from upward parabolic to downward parabolic since the electro-viscous effects are dominating as compared the pressure force. It is also noteworthy that the axial velocity topology is the classical parabolic profile for $\kappa = 1$, whereas it evolves into a flattened plug-like profile for $\kappa = 5$, and thereafter for $\kappa = 10, \rightarrow \infty$ a sharp inverse parabola is computed in the core region, although the peak velocities for these two scenarios are indistinguishable at the central section of the microchannel, whereas slightly higher axial velocity is computed near the walls for $\kappa \rightarrow \infty$.

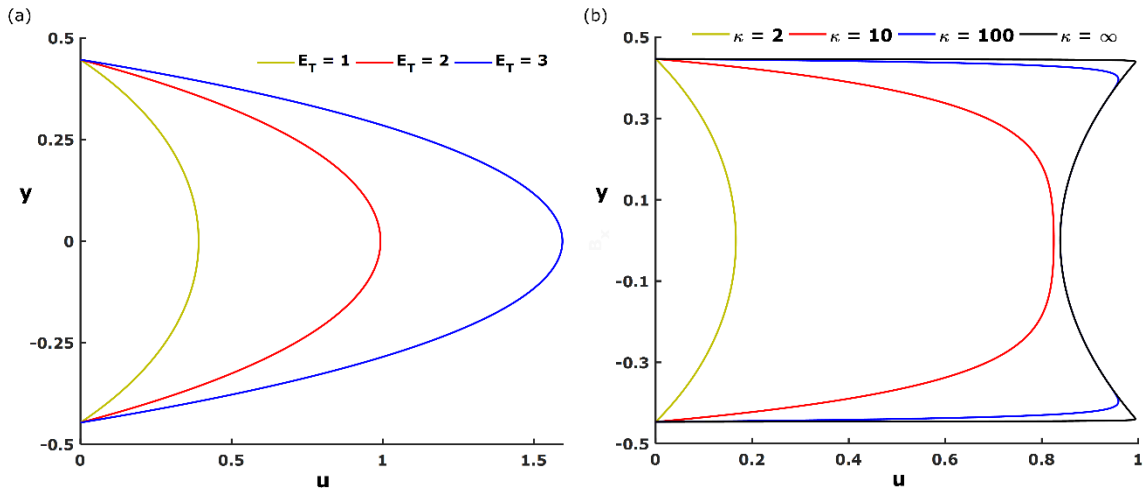

FIG. 6. The axial velocity throughout the microchannel for different values of (a) electric field parameter (b) inverse EDL thickness at fixed values of $\boldsymbol{H_a} = 3$ *and* $M = 2$.

D. Pumping characteristics

Figs. 7(a & **b)** visualize the profiles for the time-averaged volumetric flow rate at the inlet and the outlet positions for different values of (a) electric field parameter and (b) membrane shape parameter with $\boldsymbol{H_a} = 3$, and $\kappa = 1$. In the microchannel, as noted earlier, the periodic membrane motion produces the net flow, whereas the magnetic and electric parameters regulate the net flow. The result shown in **Fig. 7** represents the time average flow rate (Q_T) at the inlet position $x = -0.5$ via the solid line and at the outlet position $x = 0.5$ via the dotted line. Identical results are attained at the inlet and outlet position over a complete contraction cycle in the opposite direction i.e., $Q_T(inlet\ position,\ t = T/4) = Q_T(outlet\ position,\ t = T/4)$. Higher magnitudes of flow rate are produced consistently at the outlet (dotted lines) in both plots. **Fig. 7a** shows that with increment in electric field parameter, there is a consistent augmentation in the flow rate. This is explained by the fact that larger values of E_T correspond

to higher magnitudes of the axial driving force ($\sigma B_0 E_z$). However, an inspection of **Fig. 7b** indicates that greater values of membrane shape parameter (M) increase the net flow rate only at the outlet, whereas *at the inlet* the opposite effect is generated i.e., the flow rate is suppressed with increasing membrane shape parameter. Therefore, the membrane parameter exerts a very different effect on the transport phenomena depending on the location in the microchannel.

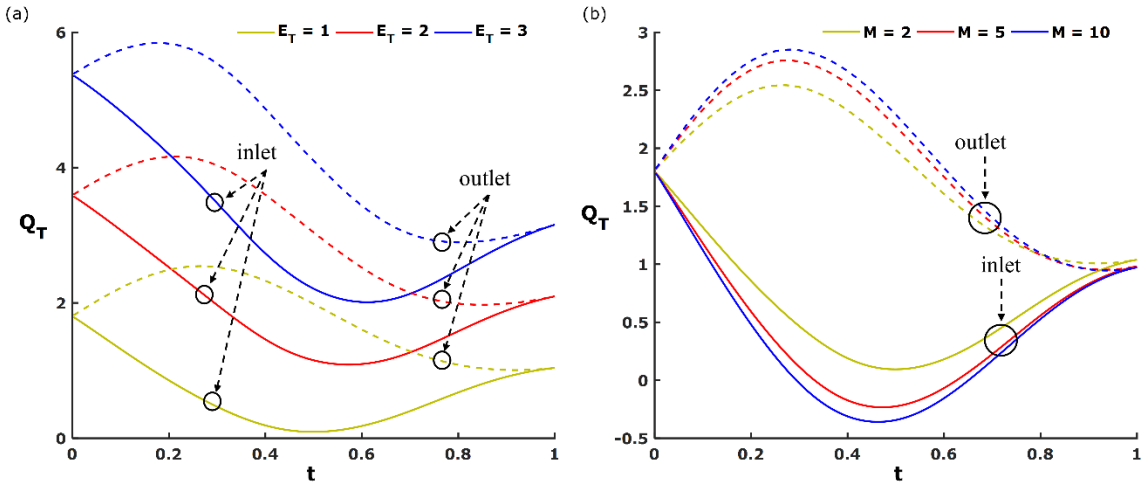

FIG. 7. Variation of the time-averaged flow rate across the length of the microchannel for different (a) electric field parameter (b) membrane shape parameter at fixed values of $\boldsymbol{H_a} = 3$ and $\kappa = 1$.

Figs. 8(a & b) depict the time-averaged flow rate vs. pressure gradient across the microchannel under the influence of (a) the electric field parameter and (b) the inverse EDL thickness at $t = T/4$ (compression phase). The plots indicate that the flow rate is *inversely proportional* to the pressure gradient i.e., a high volumetric flow rate is attained for a small pressure gradient. From **Fig. 8a**, it is evident that the Q_T is decreasing and becomes negative as the pressure gradient is increasing for $E_T = 1,2$ and 3 (i.e., backward pumping flow can be possible due to the large pressure difference). However, the positive pumping ($Q_T > 0$) is enhanced and corresponds to the strongest electric field. In addition, the variation in the time-averaged flow rate as a function of pressure gradient for three different cases (such as $\kappa = 1,\ 5, 10$) is shown in **Fig. 8b**It is noticed that the time averaged flow rate is increased with increment in κ. A positive flow rate is only guaranteed for lower pressure gradient values at any value of κ.

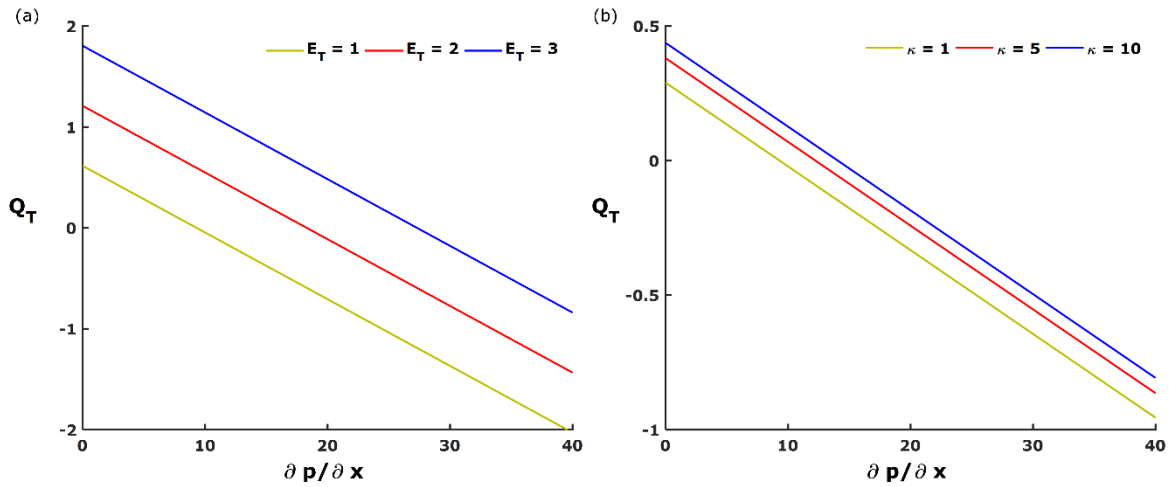

FIG. 8. Variation of the time-averaged flow rate for different (a) $E_T(= 1, 2, 3)$ and (b) $\kappa(= 1, 5, 10)$ at fixed value of $\boldsymbol{H_a} = 3$ and $M = 2$.

Physically, the magnetic force is proportional to $J \times B$, which clearly highlights the Lorentz force effect that resist the motion of fluid. For the large value of Hartman number, the magnitude of the Lorentz force is high and it leads to a small velocity in the microchannel. The minimum axial and transverse velocities magnitude is attained for $H_a = 3$ as shown in **Fig. 9(a & b)**. The membrane propagation bifurcates the axial velocity in both left and right directions, while transverse velocity is achieved near by the membrane domain. Another hand, thin EDL generates the high bulk concentration that permits a robust screening of the surface charge. From **Fig. 10**, it is observed that the electric potential is strong in the region near the wall which leads for the increment of the axial velocity. The bolus is generated in the transverse velocity which control the movement of the fluid as sketched in **Figs. 10(a & b)**. The electric body force is accumulated the axial velocity in the membrane domain with large magnitude. Further, the nature of axial velocity remains consistent to the outward direction as presented in **Fig. 11a**. Two positive and negative boluses are computed at the end of the membrane position as shown in **Fig. 11b**. These results indicate that the dependence of the axial and transverse velocities on the value of E_T is much stronger than on the value of H_a and κ.

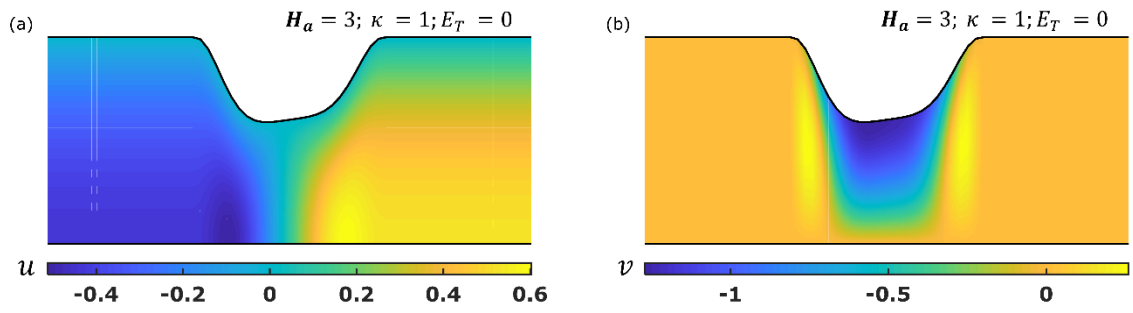

FIG. 9. The contour plot of (a) axial velocity and (b) transverse velocity without the electric field for high EDL thickness.

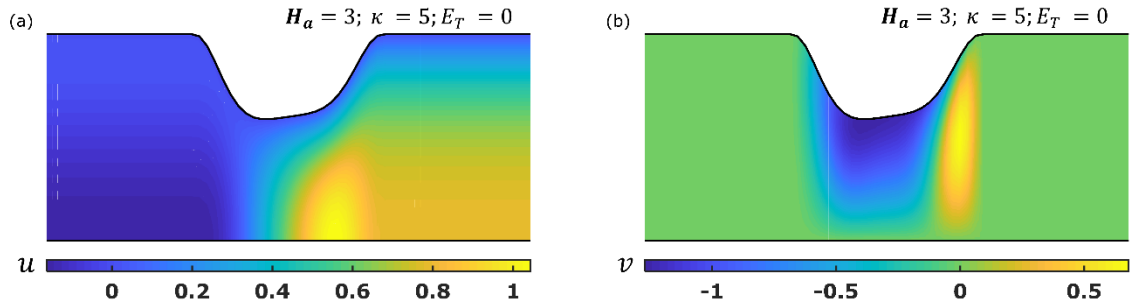

FIG. 10. The contour plot of (a) axial velocity and (b) transverse velocity component without the electric field for low EDL thickness.

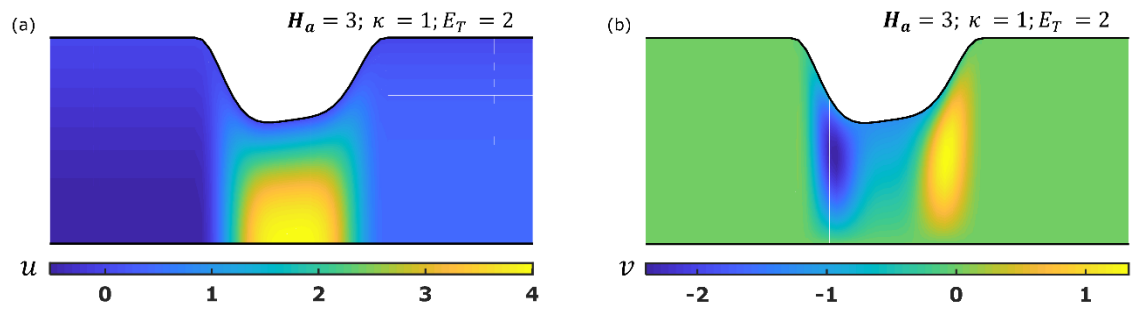

FIG. 11. The contour plot of (a) axial velocity and (b) transverse velocity with the electric field for low EDL thickness.

E. Particle tracking simulation

The particle tracking simulation method is applied based on the Lagrangian frame of reference as given in Eq. (29) to understand the instantaneous flow developed by the periodic membrane contractions inside the microchannel as depicted in **Fig. 12** and mathematically defined as:

$$\frac{d}{dt}\boldsymbol{X_p} = \boldsymbol{U_i}, \qquad \boldsymbol{X_p}(\mathbf{0}) = \boldsymbol{x_0} \tag{29}$$

where, $\boldsymbol{X_p}$ is the particle position vector and $\boldsymbol{x_0}$ describes the initial position of the particle. Here, it can be seen that how the particle is propagated in the microchannel with rhythmic membrane contraction. In the case of no electric field, initially, the particle is constantly moving as shown in **Fig. 12a**. However, the wave like movement in the particle is captured due to the membrane kinematics. This result illustrates that all the variables are linearly dependent on the pressure applied by membrane kinematics however, thin EDL thickness ($\kappa = 3$) is responsible for the small increment of the transverse direction as presented in **Fig. 12b**. In order to highlight the combined effects of magnetohydrodynamic and electroosmosis, the particle tracking results are plotted in **Fig. 12c**. It is seen that the particle ascends rapidly and progresses as high up in the y-coordinate.

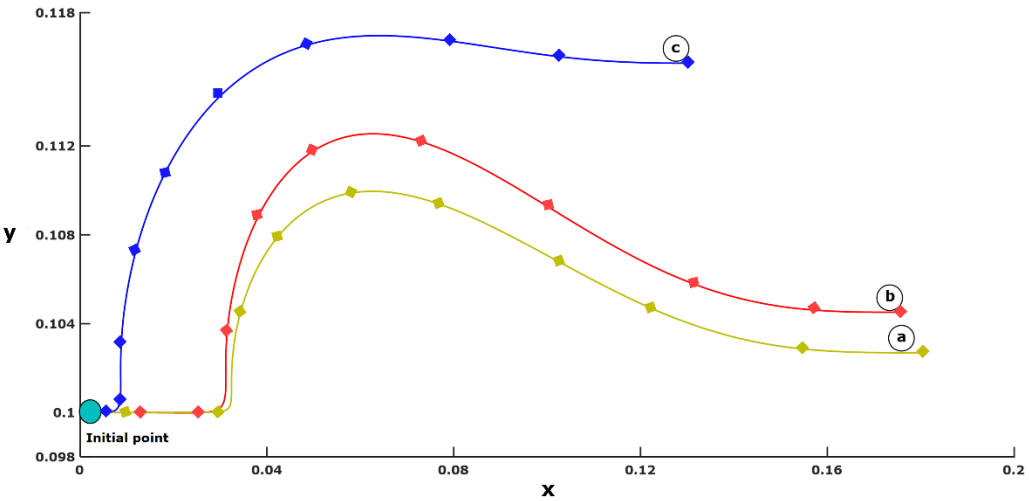

FIG. 12. Trajectory of a particle from an initial point for (a) $\kappa = 1$; $\boldsymbol{H_a} = 5; E = 0$ (b) $\kappa = 3; \boldsymbol{H_a} = 5; E = 0$ (c) $\kappa = 3$; $\boldsymbol{H_a} = 5; E_T = 2$.

lV. CONCLUSIONS

A theoretical study has been presented for the viscous flow of electro conductive fluid in a microchannel where pressure is generated by periodic membrane pumping and further amplified by both magnetohydrodynamic and electroosmotic effects. The discrete scheme

PMP i.e., periodic membrane pumping mechanism has been studied. This model is formulated based on the Navier–Stokes equations, Poisson equation, and the Maxwell electromagnetic equations and simplified for solutions subject to lubrication approximations and Debye-Hückel Linearization. The membrane kinematics induce pressure inside the microchannel to pump the fluids. The transformed dimensionless conservation equations under appropriate boundary conditions are solved analytically. Expressions are derived for axial and transverse velocities, axial pressure gradient and volumetric flow rate. The influence of key control parameters i.e. Hartmann number (transverse magnetic field), inverse EDL thickness, electrical field parameter, etc. are visualized graphically using MATLAB software. A particle tracking simulation method is also used to compute the instantaneous flow developed by the periodic membrane contractions inside the microchannel. The key findings of the present analysis are summarized as:

(i) The greater strength of the electric field elevates the net flow rate–in the microchannel.

(ii) Time- averaged flow rate is increased with decrement of EDL thickness. A positive flow rate is only guaranteed for lower pressure gradient values at any value of κ.

(iii) The electric field has much efficiency to accelerate the fluid velocity rather than inverse EDL thickness.

(iv) The magnetic parameters (H_a) enhance the fluid pressure uniformly throughout the microchannel, while E_T enforces the direction of pressure-driven flow.

(v) The electric potential is strong in the region near the wall which leads for the increment of the axial velocity.

(vi) The combined effect of electromagnetohydrodynamic elevate the particle to the transverse direction and move forward.

The present study has revealed some interesting insights into membrane pumping micro-systems combined with electromagnetohydrodynamic framework. However, attention has been confined to Newtonian ionic magnetic liquids. Future investigations may address non-Newtonian ionic magnetic liquids flow in microchannel driven by periodic membrane pumping with heat and also mass transfer.

REFERENCES

1. Jeong, Ok Chan, Sin Wook Park, Sang Sik Yang, and James Jungho Pak. "Fabrication of a peristaltic PDMS micropump." *Sensors and Actuators A: Physical* 123 (2005): 453-458.
2. Taylor, Michael T., Peter Nguyen, Jesus Ching, and Kurt E. Petersen. "Simulation of microfluidic pumping in a genomic DNA blood-processing cassette." *Journal of Micromechanics and Microengineering* 13, no. 2 (2003): 201.
3. Gong, Maojun, Ning Zhang, and Naveen Maddukuri. "Flow-gated capillary electrophoresis: a powerful technique for rapid and efficient chemical separation." *Analytical Methods* 10, no. 26 (2018): 3131-3143.
4. Forouzandeh, Farzad, Arpys Arevalo, Ahmed Alfadhel, and David A. Borkholder. "A review of peristaltic micropumps." *Sensors and Actuators A: Physical* (2021): 112602.
5. Ma, Tuo, Shixin Sun, Baoqing Li, and Jiaru Chu. "Piezoelectric peristaltic micropump integrated on a microfluidic chip." *Sensors and Actuators A: Physical* 292 (2019): 90-96.
6. Singhal, Vishal, Suresh V. Garimella, and Arvind Raman. "Microscale pumping technologies for microchannel cooling systems." *Appl. Mech. Rev.* 57, no. 3 (2004): 191-221.
7. Li, Dongqing. *Electrokinetics in microfluidics*. Elsevier, 2004.
8. Patankar, Neelesh A., and Howard H. Hu. "Numerical simulation of electroosmotic flow." *Analytical Chemistry* 70, no. 9 (1998): 1870-1881.
9. Nguyen, Nam-Trung, Steven T. Wereley, and Seyed Ali Mousavi Shaegh. *Fundamentals and applications of microfluidics*. Artech house, 2019.
10. Vasista, Kasavajhula Naga, Sumit Kumar Mehta, Sukumar Pati, and Sandip Sarkar. "Electroosmotic flow of viscoelastic fluid through a microchannel with slip-dependent zeta potential." *Physics of Fluids* 33, no. 12 (2021): 123110.
11. Hu, Zhongyan, Tianyun Zhao, Wei Zhao, Fang Yang, Hongxun Wang, Kaige Wang, Jintao Bai, and Guiren Wang. "Transition from periodic to chaotic AC electroosmotic flows near electric double layer." *AIChE Journal* 67, no. 4 (2021): e17148.
12. Mahapatra, Bimalendu, and Aditya Bandopadhyay. "Efficacy of microconfined fluid mixing in a combined electroosmotic and pressure driven transport of complex fluid over discrete electrodes." *Physics of Fluids* 34, no. 4 (2022): 042012.

13. Yang, Xu, Shaowei Wang, Moli Zhao, and Yue Xiao. "Electroosmotic flow of Maxwell fluid in a microchannel of isosceles right triangular cross section." *Physics of Fluids* 33, no. 12 (2021): 123113.
14. Mahapatra, Bimalendu, and Aditya Bandopadhyay. "Numerical analysis of combined electroosmotic-pressure driven flow of a viscoelastic fluid over high zeta potential modulated surfaces." *Physics of Fluids* 33, no. 1 (2021): 012001.
15. Huang, Hsin-Fu, and Kun-Hao Huang. "Energy efficiency analysis of mass transport enhancement in time-periodic oscillatory electroosmosis." *Physics of Fluids* 33, no. 3 (2021): 032021.
16. Pamme, Nicole. "Magnetism and microfluidics." *Lab on a Chip* 6.1 (2006): 24-38.
17. Andreozzi, Assunta, et al. "Modeling heat transfer in tumors: a review of thermal therapies." *Annals of Biomedical Engineering* 47.3 (2019): 676-693.
18. Suleman, Muhammad, and Samia Riaz. "3D in silico study of magnetic fluid hyperthermia of breast tumor using Fe3O4 magnetic nanoparticles." *Journal of Thermal Biology* 91 (2020): 102635.
19. Chouhan, Raghuraj Singh, et al. "Magnetic nanoparticles—A multifunctional potential agent for diagnosis and therapy." *Cancers* 13.9 (2021): 2213.
20. Das, Siddhartha, Suman Chakraborty, and Sushanta K. Mitra. "Magnetohydrodynamics in narrow fluidic channels in presence of spatially non-uniform magnetic fields: framework for combined magnetohydrodynamic and magnetophoretic particle transport." *Microfluidics and Nanofluidics* 13.5 (2012): 799-807.
21. Chakraborty, Suman, and Dibyadeep Paul. "Microchannel flow control through a combined electromagnetohydrodynamic transport." *Journal of Physics D: Applied Physics* 39.24 (2006): 5364.
22. Bhandari, D. S., Dharmendra Tripathi, and V. K. Narla. "Magnetohydrodynamics-based pumping flow model with propagative rhythmic membrane contraction." *The European Physical Journal Plus* 135, no. 11 (2020): 1-19.
23. Bhatti, M. M., A. Zeeshan, and R. Ellahi. "Electromagnetohydrodynamic (EMHD) peristaltic flow of solid particles in a third-grade fluid with heat transfer." Mechanics & Industry 18.3 (2017): 314.
24. Mekheimer, Kh S. "Effect of the induced magnetic field on peristaltic flow of a couple stress fluid." *Physics Letters A* 372.23 (2008): 4271-4278.

25. Akbar, Noreen Sher, M. Raza, and R. Ellahi. "Influence of induced magnetic field and heat flux with the suspension of carbon nanotubes for the peristaltic flow in a permeable channel." *Journal of magnetism and magnetic materials* 381 (2015): 405-415.
26. Sarkar, Sandip, Suvankar Ganguly, and Suman Chakraborty. "Influence of combined electromagnetohydrodynamics on microchannel flow with electrokinetic effect and interfacial slip." *Microfluidics and Nanofluidics* 21.3 (2017): 1-16.
27. Tripathi, Dharmendra, *et al*. "Electro-magneto-hydrodynamic peristaltic pumping of couple stress biofluids through a complex wavy micro-channel." *Journal of Molecular Liquids* 236 (2017): 358-367.
28. Saha, Kalyan, P. V. S. N. Murthy, and Suman Chakraborty. "Rheology-modulated alterations in electro-magneto-hydrodynamic flows in a narrow cylindrical capillary: Contrasting trends in high and low surface charge limits." *Electrophoresis* 43, no. 5-6 (2022): 732-740.
29. Moradmand, A., M. Saghafian, and B. Moghimi Mofrad. "Electroosmotic pressure-driven flow through a slit micro-channel with electric and magnetic transverse field." *Journal of Applied Fluid Mechanics* 12.3 (2019): 961-969.
30. Ramesh, K., D. Tripathi, M. M. Bhatti, and C. M. Khalique. "Electro-osmotic flow of hydromagnetic dusty viscoelastic fluids in a microchannel propagated by peristalsis." *Journal of Molecular Liquids* 314 (2020): 113568.
31. Prakash, J., Alok K. Ansu, and D. Tripathi. "Alterations in peristaltic pumping of Jeffery nanoliquids with electric and magnetic fields." *Meccanica* 53, no. 15 (2018): 3719-3738.
32. Aboelkassem, Yasser, and Anne E. Staples. "A bioinspired pumping model for flow in a microtube with rhythmic wall contractions." *Journal of Fluids and Structures* 42 (2013): 187-204.
33. Aboelkassem, Yasser. "Pumping flow model in a microchannel with propagative rhythmic membrane contraction." *Physics of Fluids* 31.5 (2019): 051902.
34. Bhandari, D. S., Dharmendra Tripathi, and V. K. Narla. "Pumping flow model for couple stress fluids with a propagative membrane contraction." *International Journal of Mechanical Sciences* 188 (2020): 105949.
35. Tripathi, Dharmendra, V. K. Narla, and Yasser Aboelkassem. "Electrokinetic membrane pumping flow model in a microchannel." *Physics of Fluids* 32, no. 8 (2020): 082004.

36. Bhandari, D. S., Dharmendra Tripathi, and J. Prakash. "Insight into Newtonian fluid flow and heat transfer in vertical microchannel subject to rhythmic membrane contraction due to pressure gradient and buoyancy forces." *International Journal of Heat and Mass Transfer* 184 (2022): 122249.
37. Saha, Kalyan, P. V. S. N. Murthy, and Suman Chakraborty. "Rheology-modulated alterations in electro-magneto-hydrodynamic flows in a narrow cylindrical capillary: Contrasting trends in high and low surface charge limits." *Electrophoresis* 43, no. 5-6 (2022): 732-740.
38. Moradmand, A., M. Saghafian, and B. Moghimi Mofrad. "Electroosmotic pressure-driven flow through a slit micro-channel with electric and magnetic transverse field." *Journal of Applied Fluid Mechanics* 12.3 (2019): 961-969.